

## Article

# Study on Thermal Runaway Behavior and Jet Characteristics of a 156 Ah Prismatic Ternary Lithium Battery

Huipeng Zhang

Department of Mechanical and Electronic Engineering, Yuncheng University, Yuncheng 044000, China; zhanghuipeng2024@126.com

**Abstract:** Ternary lithium batteries have been widely used in transportation and energy storage due to their high energy density and long cycle life. However, safety issues arising from thermal runaway (TR) need urgent resolution. Current research on thermal runaway in large-capacity ternary lithium batteries is limited, making the study of hazard indicators during the thermal runaway ejection process crucial. This study places a commercial 156 Ah prismatic battery (positive electrode material:  $\text{Li}(\text{Ni}_{0.8}\text{Mn}_{0.1}\text{Co}_{0.1})\text{O}_2$ , negative electrode material: graphite) in a nitrogen-filled sealed container, triggering thermal runaway through lateral heating. The experimental results show that the battery's maximum surface temperature can reach  $851.8\text{--}943.7\text{ }^\circ\text{C}$ , exceeding the melting point of aluminum. Temperature surge inflection points at the battery's bottom and near the small side of the negative electrode coincide with the inflection point on the heated surface. The highest jet temperatures at three monitoring points 50 mm, 150 mm, and 250 mm above the safety valve are  $356.9\text{ }^\circ\text{C}$ ,  $302.7\text{ }^\circ\text{C}$ , and  $216.5\text{ }^\circ\text{C}$ , respectively. Acoustic signals reveal two ejection events. The average gas production of the battery is 0.089 mol/Ah, and the jet undergoes three stages: ultra-fast ejection (2 s), rapid ejection (32 s), and slow ejection (47 s). Post-thermal runaway remnants indicate that grooves from internal jet impacts are mainly located at  $\pm 45^\circ$  positions. This study provides valuable insights for the safety design of batteries and the suppression of thermal runaway propagation.

**Keywords:** ternary lithium batteries; thermal runaway; jet characteristics



**Citation:** Zhang, H. Study on Thermal Runaway Behavior and Jet Characteristics of a 156 Ah Prismatic Ternary Lithium Battery. *Batteries* **2024**, *10*, 282. <https://doi.org/10.3390/batteries10080282>

Academic Editor: Mingyi Chen

Received: 16 June 2024

Revised: 22 July 2024

Accepted: 29 July 2024

Published: 6 August 2024



**Copyright:** © 2024 by the author. Licensee MDPI, Basel, Switzerland. This article is an open access article distributed under the terms and conditions of the Creative Commons Attribution (CC BY) license (<https://creativecommons.org/licenses/by/4.0/>).

## 1. Introduction

In recent years, with the depletion of global fossil energy resources, new energy sources represented by lithium-ion batteries (LIBs) have been widely applied in the fields of transportation and energy storage. Among various types of lithium batteries, ternary lithium batteries, whose cathode materials consist of nickel, cobalt, and manganese, have become an essential part of modern energy storage technology due to their high energy density, long cycle life, and low self-discharge rate [1–4]. As battery technology advances, the application scope of ternary lithium batteries is expected to expand further [5].

However, there are still many safety issues with ternary lithium batteries that need urgent resolution [6–9]. In recent years, incidents of fires and explosions caused by battery thermal runaway have occurred frequently. For instance, in 2023, the New York Fire Department handled 267 fire incidents caused by thermal runaway of lithium-ion batteries, resulting in 150 injuries and 18 deaths [10]. Accident investigations have shown that lithium batteries are highly likely to trigger thermal runaway when subjected to mechanical crush, overcharging, internal short circuits, and high-temperature environments [11–17]. Ternary lithium batteries have high energy density and generate significant heat during thermal runaway, with faster heat propagation rates within the battery modules, leading to more severe fire incidents [18]. Lithium batteries are composed of cathode materials, anode materials, copper current collectors, aluminum current collectors, separators, electrolytes, aluminum casings, and safety valves, with the electrolyte and electrode materials being flammable [16,19–21]. During thermal runaway, reactions between the cathode and anode

materials and the electrolyte produce large amounts of flammable gases such as CO, H<sub>2</sub>, CH<sub>4</sub>, and C<sub>2</sub>H<sub>4</sub> [22–24], releasing a significant amount of heat that causes the safety valve to open. This results in combustible gases, electrolyte, and electrode materials coming into contact with air, leading to intense combustion and flame jets [25–27].

Currently, numerous scholars are conducting extensive research on the mechanisms of thermal runaway and fire behaviors of ternary lithium batteries. Wei et al. studied the effects of different abuse methods on thermal runaway behavior using an embedded thermocouple and an accelerating rate calorimeter (EV-ARC) with Li(Ni<sub>0.5</sub>Co<sub>0.2</sub>Mn<sub>0.3</sub>)O<sub>2</sub> as the cathode material and graphite as the anode material. They triggered thermal runaway using three methods: puncture, overcharging, and side heating, with internal battery temperatures reaching 994.8, 964.3, and 1020 °C, respectively. Observations indicated that overcharging-induced thermal runaway caused the most severe battery damage [28].

Ohneseit et al. conducted a study on the thermal runaway behavior of 21,700 batteries at different states of charge (SOC) using an EV-ARC. The batteries had a cathode material of Li(Ni<sub>0.8</sub>Co<sub>0.1</sub>Mn<sub>0.1</sub>)O<sub>2</sub> and a capacity of 4950 mAh. The results showed that at 0% SOC, the batteries did not undergo thermal runaway, while at 30% SOC, 50% SOC, and 100% SOC, thermal runaway occurred [29].

Han et al. performed thermal runaway propagation experiments on aged batteries using a self-made box. The subjects were 1880 mAh ternary lithium batteries. The results indicated that, at room temperature, the thermal runaway onset temperature and temperature change rate of batteries with a state of health (SOH) of 90% were lower than those of fresh batteries, but the mass loss was significantly greater [30].

Previous studies mainly focused on methods for triggering thermal runaway in small-capacity batteries [31,32], the impact of SOC [33–36], and SOH [31,37–41] on thermal runaway. There is relatively less research on large-capacity high-nickel NCM batteries, and jet studies specifically targeting NCM batteries are also rare. Therefore, this study investigates the surface temperature and jet characteristics of large-capacity NCM batteries during thermal runaway. The experiments were conducted in a nitrogen atmosphere with 99.75% concentration. The battery's cathode material was Li(Ni<sub>0.8</sub>Co<sub>0.1</sub>Mn<sub>0.1</sub>)O<sub>2</sub>, the anode material was graphite, and the capacity was 156 Ah. The experiments were carried out in a 1000 L container, with thermocouples monitoring the surface temperatures at five positions (front, back, left, right, and bottom) of the battery, jet temperatures at three positions (50, 150, and 250 mm above the safety valve), and ambient temperatures at four positions within the test chamber. Pressure sensors were used to monitor the gas production in real time, and cameras and recording devices were employed to observe the characteristics during the battery ejection process. This study aims to provide references for battery safety design and fire warning systems.

## 2. Materials and Methods

### 2.1. Battery Samples

The subject of this experiment is a large-capacity commercial prismatic lithium-ion battery with a rated capacity of 156 Ah. The cathode material is Li(Ni<sub>0.8</sub>Co<sub>0.1</sub>Mn<sub>0.1</sub>)O<sub>2</sub>, and the anode material is graphite. The cathode current collector is aluminum foil, while the anode current collector is copper foil. The energy density is 248.00 Wh/kg, and the discharge energy is 572.00 Wh. The nominal voltage is 3.65 V. The charging cut-off voltage is 4.2 V, and after resting for 24 h, the stabilized voltage is 4.146 V. The discharging cut-off voltage is 2.8 V. The operating voltage range is 2.8 to 4.2 V. The internal resistance of the battery is less than or equal to 0.6 mΩ. The operating temperature range under discharge conditions is –30 to 55 °C, and under charging conditions, it is –20 to 55 °C. The weight of the battery is 2287 ± 25 g. The main performance parameters of the battery provided by the manufacturer are shown in Table 1 below.

**Table 1.** Basic Parameters of the Battery to be tested.

Item	Specification	Condition
Nominal Capacity	156 Ah	25 °C, 52 A(1/3C) DC to 2.8 V
Energy	572 Wh	25 °C, 52 A(1/3C) DC to 2.8 V
Specific Energy	248.00 Wh/Kg	25 °C, 52 A(1/3C) DC to 2.8 V
Operating voltage	2.8~4.2 V	-30 °C ≤ T ≤ 55 °C
Cathode	Li(Ni <sub>0.8</sub> Co <sub>0.1</sub> Mn <sub>0.1</sub> )O <sub>2</sub>	N.A.
Anode	Graphite	N.A.
Standard Voltage	3.637 ± 0.01 V	25 °C, BOL, 40% SOC
Operating temperature (Charge)	-20~55 °C	N.A.
Operating temperature (discharge)	-30~55 °C	N.A.
Cycle life	≥1500	25 °C, 1C/1C, 5–97% SOC, 80% SOH
discharge power	≥2100 W	25 °C, 50% SOC, 10 s
Discharge power density	≥912 W/Kg	25 °C, 50% SOC, 10 s
SOC	100%	N.A.
Cell weight	2287 ± 25 g	N.A.
Cell dimension	220 × 102 × 45 mm	N.A.
Shell Material	Aluminum alloy	N.A.

## 2.2. Experimental Equipment

The primary equipment used in this study is a self-made sealed pressure vessel with a capacity of 1000 L. Its basic components include the chamber, signal acquisition system, gas intake and exhaust system, and thermal runaway trigger system. Figure 1 shows the composition of the experimental equipment.

The sealed chamber is cylindrical in shape. It has a circular sealing door on the side, which is secured to the chamber body with bolts. Both the chamber body and the sealing door are made of Q345R material, with a maximum pressure capacity of 2 MPa.

The signal acquisition system includes pressure sensors inside the chamber, temperature sensors, voltage signal sensors, and a camera system. An absolute pressure sensor is mounted on the equipment door, with a range of 0–200 KPa and an accuracy of ±0.2%FS. Its function is to measure pressure changes in the container before, during, and after the battery thermal runaway. Fifteen K-type armored thermocouples are installed on the sealed chamber door, with a range of -200 °C to 1300 °C. The thermocouples measure the temperature at various positions on the battery, the ambient temperature inside the chamber, and the temperature of the ejected gases. Voltage acquisition lines with alligator clips are also installed on the sealed chamber door to clamp onto the battery terminals and collect voltage signals in real time. The TP700 multi-channel data recorder displays and stores data from the absolute pressure sensor, K-type armored thermocouples, and voltage acquisition lines, and uploads the data to a computer for analysis. A camera with charging capabilities and recording equipment is installed inside the chamber. The camera has six fill lights on its side, a battery capacity of 2500 mAh, and can operate continuously for 18 h. It has 128 Gb of storage space, a resolution of 1920 P, and can capture 30 frames per second. Its function is to record the ejection phenomena during the battery thermal runaway process. The camera can be reused. The specific protection method involves attaching a 3 mm glass sheet to the camera using Teflon tape to protect the camera lens. In addition to the lens area, the rest of the camera is covered with two layers of Teflon tape to isolate heat and protect the camera body.

The gas intake and exhaust system includes a nitrogen source, intake valve, exhaust valve, and vacuum pump. The nitrogen source is provided by a pure nitrogen cylinder with a purity of 99.9%. When the intake valve is manually opened, nitrogen can be charged into the sealed chamber. After manually closing the intake valve and opening the exhaust valve, the vacuum pump can evacuate the mixed gases from the chamber.

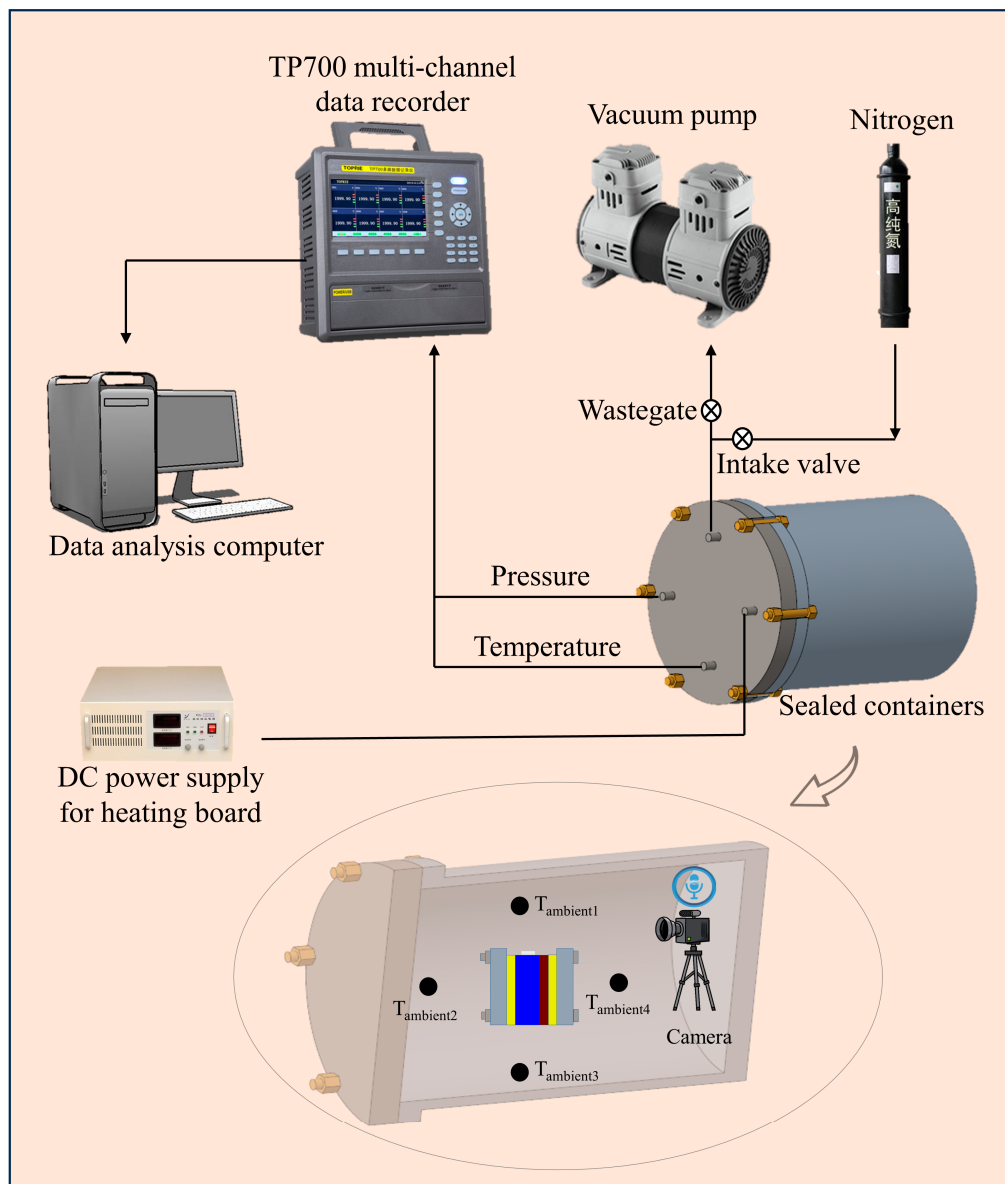


**Figure 1.** Experimental equipment.

The thermal runaway trigger system includes specialized aluminum alloy clamps, mica insulating boards, electric heating plates, bolts, and nuts. The functions of the specialized aluminum alloy clamps include: (1) According to China's GB 38031-2020 "Electric vehicles traction battery safety requirements", the electric heating plate is closely attached to the battery, allowing the heat generated by the electric heating plate to quickly transfer into the battery, triggering thermal runaway. (2) securely installing thermocouples via bolt connections between the two aluminum alloy clamp planes, preventing them from falling off during thermal runaway. The mica insulating board, with a thickness of 3 mm, insulates heat transfer, ensuring most of the heat generated by the heating plate is conducted into the battery. The resistance of the electric heating plate is between  $91.8 \Omega$  and  $93.8 \Omega$ . A DC power supply is used to power the heating plate, maintaining a heating power of 400 W. According to the research by Jin and Ouyang et al., when lateral heating triggers thermal runaway in a battery, the greater the power of the heating plate per unit area, the faster the thermal runaway trigger rate [42]. In this study, a lower power 400 W heating plate was selected. The battery can absorb more heat from the heating plate before

thermal runaway, resulting in a more intense thermal runaway process. This simulates the maximum hazard level during thermal propagation between adjacent batteries.

### 2.3. Experimental Procedure

1. Preparation: Charge the 156 Ah NCM811 battery to 100% SOC (State of Charge) at 0.1 C using a battery charge-discharge machine (model NEWARE BTS4000-5V30A) and let it rest for 24 h;
2. Thermocouple Installation: Fix K-type armored thermocouples to the battery surface using polyimide and Teflon tapes at the temperature monitoring points shown in Figure 2b,c. Special attention should be paid to the thermocouple near the heating plate. First, fix it with a layer of polyimide tape, and then attach two layers of Teflon tape to prevent the thermocouple from coming into direct contact with the heating plate. This ensures that the thermocouple measures the battery surface temperature rather than the surface temperature of the heating plate. Clamp the battery as shown in Figure 2a and use a torque wrench to pre-tighten the fastening bolts to 1 N·m.

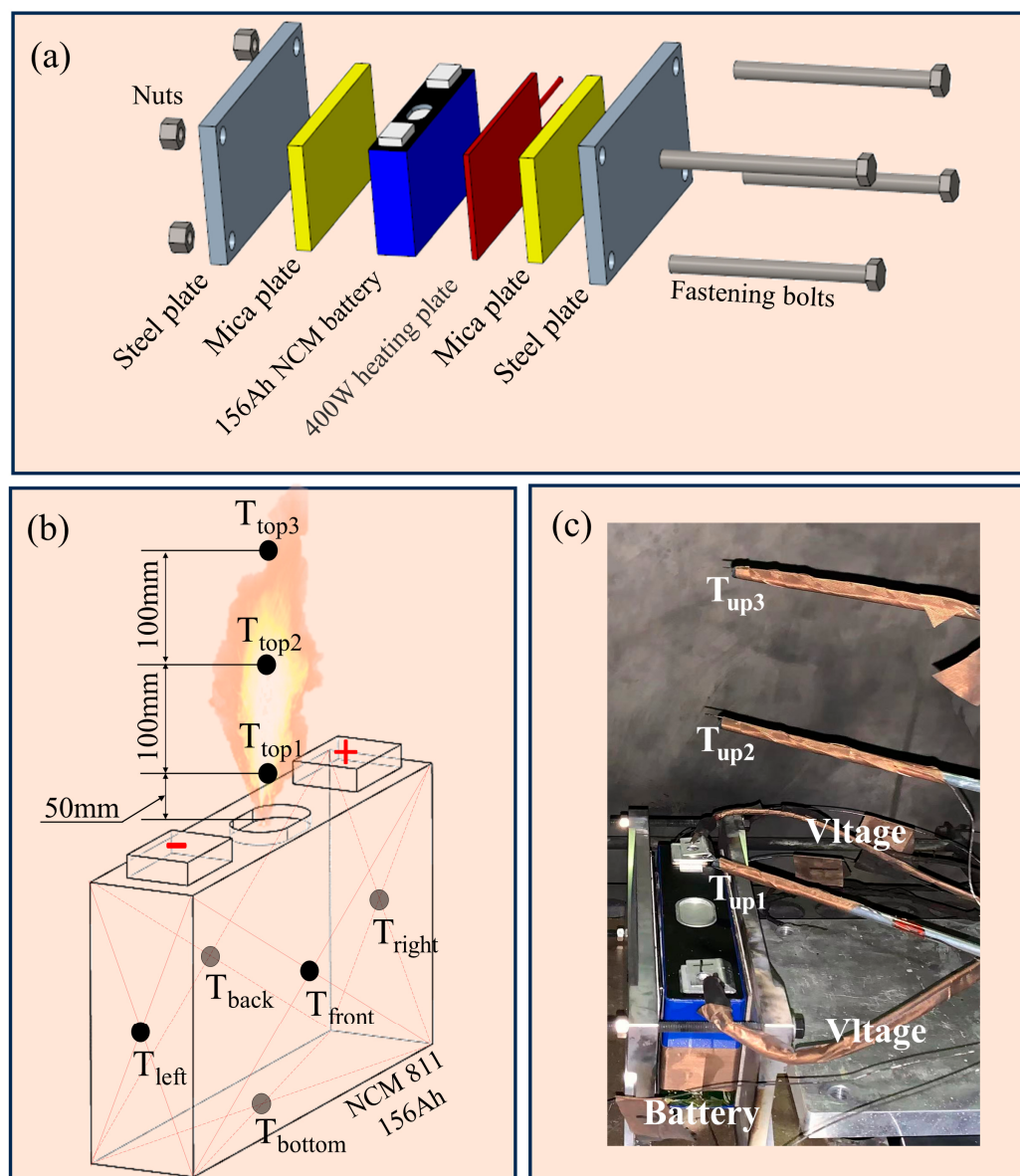


**Figure 2.** Battery installation. (a) Battery clamping structure. (b) Thermocouple placement locations. (c) Actual thermocouple placement.

1. Place the clamped battery in a custom-made sealed pressure vessel with a capacity of 1000 L. The top of the battery should be approximately 800 mm from the top of the experimental chamber. Adjust the positions of the four environmental monitoring thermocouples on all sides (top, bottom, left, and right), and start the camera. Close the pressure vessel door and lock the bolts;
2. Nitrogen Purging: Ensure both the intake and exhaust valves are initially closed. At the start of the test, open the exhaust valve and turn on the vacuum pump to evacuate the air inside the chamber. When the pressure drops to 5 Kpa, close the exhaust valve and turn off the vacuum pump. Open the intake valve to fill the chamber with nitrogen until the pressure reaches 101 Kpa, then close the intake valve. Repeat this process three times to reduce the oxygen concentration in the chamber to 0.0025%, ensuring the chamber is filled with 99.75% nitrogen;
3. Triggering Thermal Runaway: Turn on the heating plate power supply and maintain the heating plate at a power of 400 W. Monitor the battery voltage data; when the voltage drops to 0 V, immediately turn off the heating plate power supply, indicating that thermal runaway has been triggered;
4. Post-Experiment Procedure: After the battery temperature inside the chamber drops to room temperature, open the chamber door, collect the solid substances ejected during thermal runaway, and clean the chamber;
5. Repetition: Repeat the above process for a total of three experiments.

### 3. Experimental Results and Analysis

#### 3.1. Battery Surface Temperature and Voltage Changes

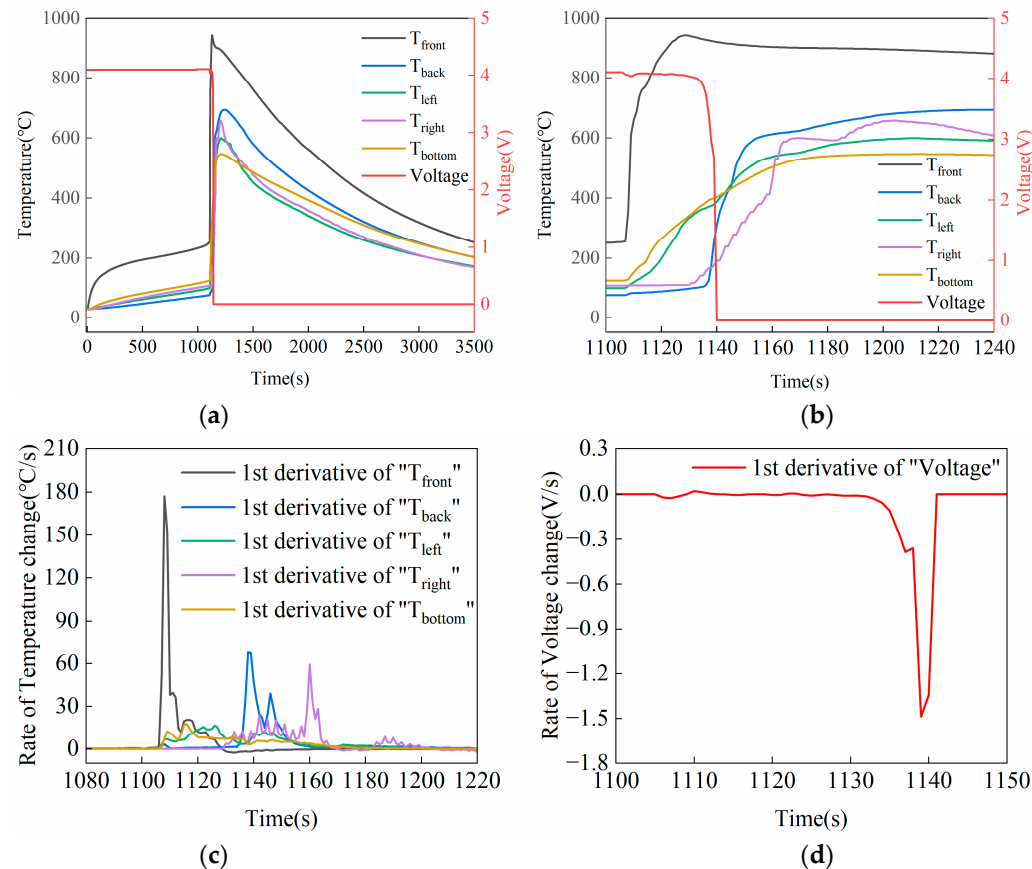
During thermal runaway, the battery surface temperature undergoes significant changes [18,43,44]. To measure the temperature at various surfaces during thermal runaway, thermocouples were attached to the center of the front, back, left, right, and bottom surfaces of the battery.

Figure 3a shows the changes in surface temperature and voltage during the first experiment with thermal runaway. The battery was heated with a 400 W heating plate, causing a gradual accumulation of heat. The temperatures at all monitoring points increased steadily. When the temperature on the front surface ( $T_{front}$ ) reached 257.2 °C, the surface temperature began to rise rapidly, indicating the onset of severe thermal runaway. The internal battery generated a large amount of gas, leading to the opening of the safety valve, and the highest recorded temperature reached 943.7 °C. This suggests that a significant amount of heat was generated during the decomposition of the electrolyte and the short-circuiting process inside the battery during thermal runaway [45–47]. Concurrently, the battery voltage dropped sharply to 0. Compared to the findings of Shen et al. [5,48], the maximum temperature observed in this study was higher, likely due to the larger battery capacity, which resulted in longer chemical reaction times and more heat generation, leading to higher temperatures. Therefore, it can be inferred that the larger the battery capacity, the greater the heat generation during thermal runaway and the higher the temperature.

Figure 3b illustrates the surface temperature of the battery during the thermal runaway ejection phase. At 1107 s, the  $T_{front}$  rapidly increased, marking the start of the severe thermal runaway phase. At 1136 s, the temperature at the back surface ( $T_{back}$ ) began to rise quickly, indicating that the thermal runaway front had reached the back of the battery [49]. At 1140 s, the voltage dropped to 0, signifying the complete reaction of the active materials within the battery. The propagation of thermal runaway from the front surface to the back surface took a total of 29 s. Given the battery's thickness of 45 mm, the propagation speed of thermal runaway within the battery can be calculated using Equation (1) as 0.00155 m/s.

$$v_{incell} = \frac{h}{t} \times 0.001 \quad (1)$$

$V_{incell}$  represents the propagation speed of thermal runaway within the battery, measured in m/s;  $h$  represents the battery thickness, measured in mm;  $t$  represents the duration of thermal runaway, measured in seconds.



**Figure 3.** Battery surface temperature during the first experiment. **(a)** Battery surface temperature. **(b)** Battery surface temperature during thermal runaway ejection. **(c)** Rate of change in battery surface temperature. **(d)** Rate of change in voltage.

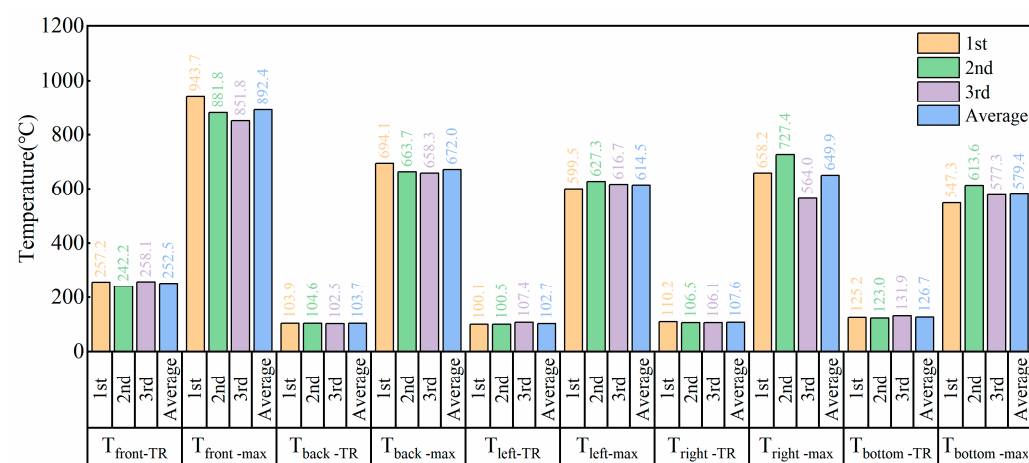
Figure 3c shows the temperature rise rate at various monitoring points, with the highest rate observed at Derivative ( $T_{front}$ ), reaching  $177.15\text{ }^{\circ}\text{C/s}$ . This is because the continuous heat input from the heating plate causes more intense thermal runaway reactions at high temperatures, resulting in a higher heat release rate. The lowest temperature rise rate is at Derivative ( $T_{bottom}$ ), only  $17.8\text{ }^{\circ}\text{C/s}$ , indicating good temperature uniformity. This is because the electrolyte inside the battery evenly distributes the heat generated by thermal runaway to the bottom surface, and the evaporation of the electrolyte also carries away a significant amount of heat. The order of the temperature rise rates at the monitoring points is: Derivative ( $T_{front}$ ) > Derivative ( $T_{back}$ ) > Derivative ( $T_{right}$ ) > Derivative ( $T_{left}$ ) > Derivative ( $T_{bottom}$ ). The Derivative ( $T_{left}$ ) and Derivative ( $T_{right}$ ) exhibit two peak groups due to the two wound cores inside the battery, with thermal runaway propagating from one core to the other sequentially. The order of the appearance of the thermal runaway inflection points  $T_{x-TR}$  (where the temperature rise rate exceeds  $3\text{ }^{\circ}\text{C/s}$ ) is: Time( $T_{front}$ ) = Time( $T_{bottom}$ ) = Time( $T_{left}$ ) < Time( $T_{right}$ ) < Time( $T_{back}$ ), indicating that the direction of thermal runaway propagation is from the heated side to the non-heated side, and from the anode side to the cathode side.

Figure 3d shows the rate of voltage change during the battery's thermal runaway. At the start of the thermal runaway ejection phase, the voltage fluctuated for 33 s but remained mostly unchanged. When the thermal runaway front reached the non-heated side, the voltage began to drop sharply, decreasing from  $4.0\text{ V}$  to  $0\text{ V}$  within 6 s. This indicates that

the battery voltage remains relatively stable during the ejection phase of thermal runaway and only experiences a sharp decline when the thermal runaway front reaches the back of the battery [50].

- $T_{X-TR}$ : Inflection point temperature at the monitoring point (temperature rise rate greater than  $3\text{ }^{\circ}\text{C/s}$ ).
- $T_{X-max}$ : Maximum temperature at the monitoring point.

Figure 4 shows the inflection point temperatures and maximum temperatures at each monitoring point across three experiments [51], along with the calculated average values for the three experiments. The average maximum inflection point temperature on the heated side (front),  $T_{front-TR}$ , is  $252.5\text{ }^{\circ}\text{C}$ , due to the direct heating effect of the heating plate. The inflection point temperature at the bottom of the battery ranks second at  $126.7\text{ }^{\circ}\text{C}$ . This may be because the bottom of the battery is directly placed on a mica plate, resulting in no heat conduction with the air. The temperatures on the left and right sides of the battery are lower because they are exposed to air, creating thermal convection and causing some heat loss. The back of the battery has a relatively low temperature due to its distance from the heat source, leading to significant heat loss during heat transfer. The inflection point temperatures at the back, left, and right sides of the battery are nearly identical, at  $103.7\text{ }^{\circ}\text{C}$ ,  $102.7\text{ }^{\circ}\text{C}$ , and  $107.6\text{ }^{\circ}\text{C}$ , respectively. The order of the highest temperatures at the six monitoring points from highest to lowest is:  $T_{front-max} > T_{back-max} > T_{right-max} > T_{left-max} > T_{bottom-max}$ . This indicates that the largest surfaces of the battery have the highest temperatures due to the maximum contact area with the wound cores, resulting in efficient heat conduction. Since the copper current collector has better thermal conductivity than the aluminum current collector, the small surface near the cathode has a higher temperature than the small surface near the anode. The bottom surface of the battery has the lowest  $T_{bottom-max}$  temperature due to the heat conduction and heat absorption by the electrolyte's evaporation.



**Figure 4.** Inflection point temperature and maximum temperature at each monitoring point in three experiments.

### 3.2. Battery Thermal Runaway Jet Temperature

To measure the temperature of the thermal runaway jet of the battery, three temperature monitoring points were set up at 50 mm, 150 mm, and 250 mm above the safety valve. Figure 5 shows the temperature monitoring of the thermal runaway jet of the battery.

Figure 5 shows the temperature monitoring of the battery thermal runaway jet during the first experiment. Figure 5a–c display the temperatures at three monitoring points across three experiments. The temperature is highest at the 50 mm position from the nozzle, ranging from  $351.6\text{ }^{\circ}\text{C}$  to  $364.2\text{ }^{\circ}\text{C}$ . The temperature is lowest at the 250 mm position from the nozzle, ranging from  $175.3\text{ }^{\circ}\text{C}$  to  $216.5\text{ }^{\circ}\text{C}$ . The temperature at the middle monitoring point fluctuates between  $229.8\text{ }^{\circ}\text{C}$  and  $302.7\text{ }^{\circ}\text{C}$ . This indicates that the further away from

the outlet, the lower the jet temperature. This is because there are no continuous heat-producing substances within the jet, causing the heat within the jet to dissipate rapidly into the environment, thus gradually lowering the jet temperature [52–55].

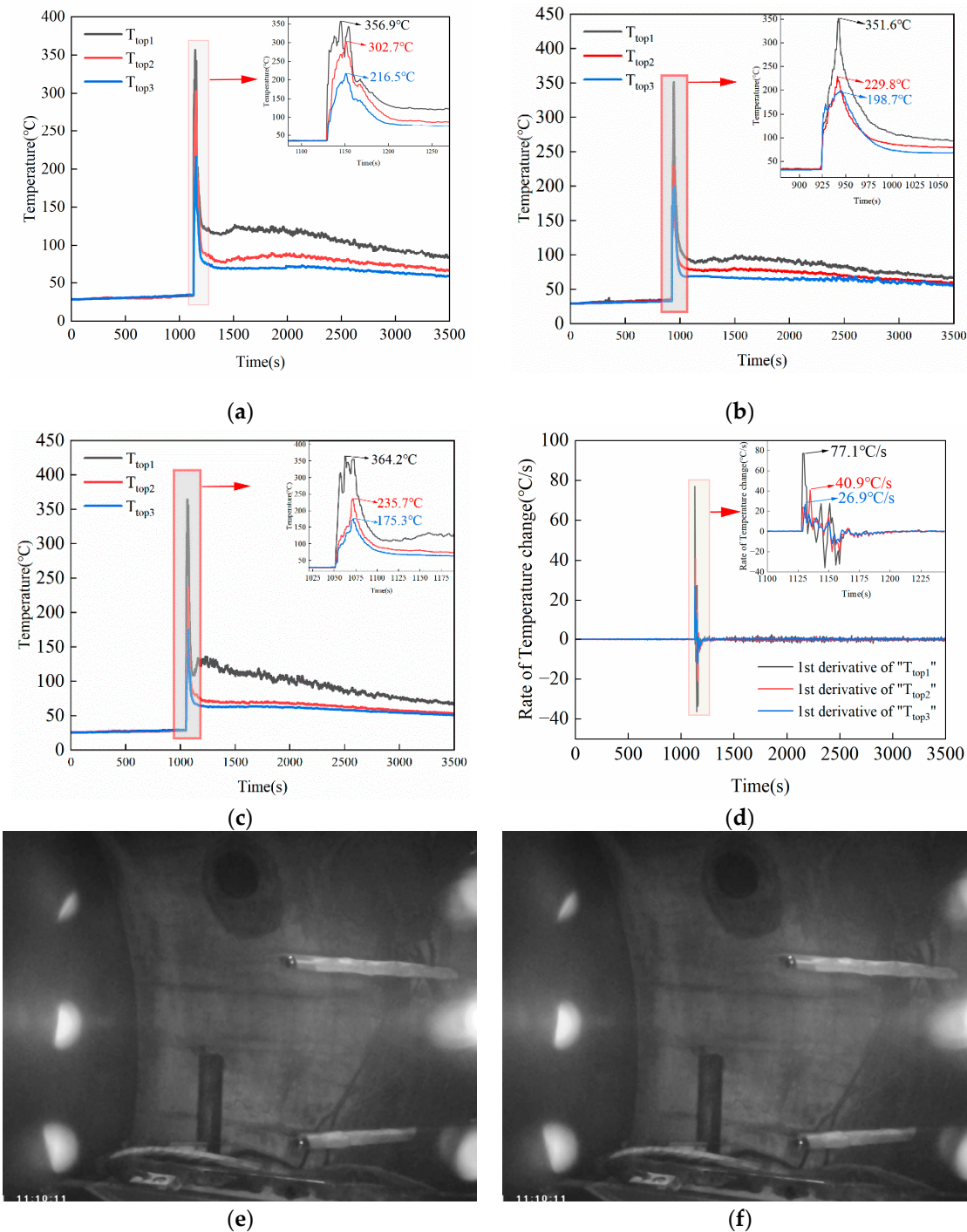


**Figure 5.** Temperature of Battery Thermal Runaway Jet (a) Temperature at monitoring points 50 mm, 150 mm, and 250 mm above the battery nozzle during the first experiment. (b) Temperature at monitoring points 50 mm, 150 mm, and 250 mm above the battery nozzle during the second experiment. (c) Temperature at monitoring points 50 mm, 150 mm, and 250 mm above the battery nozzle during the third experiment. (d) Rate of temperature change at monitoring points 50 mm, 150 mm, and 250 mm above the battery nozzle during the first experiment. (e) Image before thermal runaway. (f) Image of the jet at the initial stage of thermal runaway.

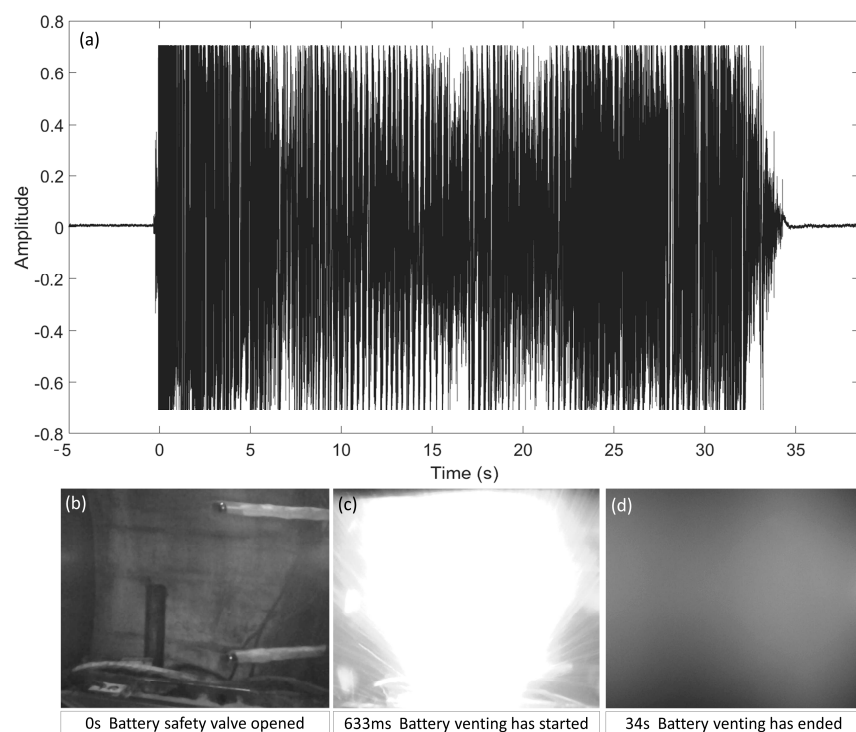
Figure 5d shows the rate of temperature change at the three monitoring points during the first experiment. The maximum temperature rise rates at the positions 50 mm, 150 mm, and 250 mm from the safety valve were  $77.1\text{ }^{\circ}\text{C/s}$ ,  $40.9\text{ }^{\circ}\text{C/s}$ , and  $26.9\text{ }^{\circ}\text{C/s}$ , respectively. The temperature change rate is inversely proportional to the distance from the outlet. This is because, during the jet ejection process, the jet expands in multiple directions. The further the distance from the outlet, the less thermal energy-containing jet reaches the monitoring point, resulting in lower temperatures [56,57].

Measuring the jet temperature during thermal runaway is challenging because the shape of the jet often changes. Golubkov et al. (2018) used a fixed device for directional jetting and placed a thermocouple offset from the centerline, resulting in higher measured temperatures compared to most other studies on inert gas emissions [58]. This study focuses on the thermal runaway jet of batteries in a nitrogen atmosphere. Experiments revealed that during the initial phase of battery thermal runaway ejection, the jet direction is not directly upward due to the internal structure of the battery.

As seen in the images captured by the camera in Figure 5e,f, the initial jet forms an angle of approximately 45 degrees with the battery. Thus, thermocouples placed directly above the battery cannot effectively capture the initial jet temperature. As thermal runaway progresses and the internal structure of the battery is damaged, the jet eventually ejects directly upwards, allowing the thermocouples to measure the temperature during the latter part of the ejection process.

### 3.3. Video and Audio Signals during the Battery Thermal Runaway Ejection Process

To investigate the changes in video and audio signals during the battery ejection process [59], night vision cameras and recording equipment were used to monitor the thermal runaway process of the battery. The camera recorded images in night vision mode, resulting in black and white images. Figure 6 shows the audio signals and thermal runaway images.



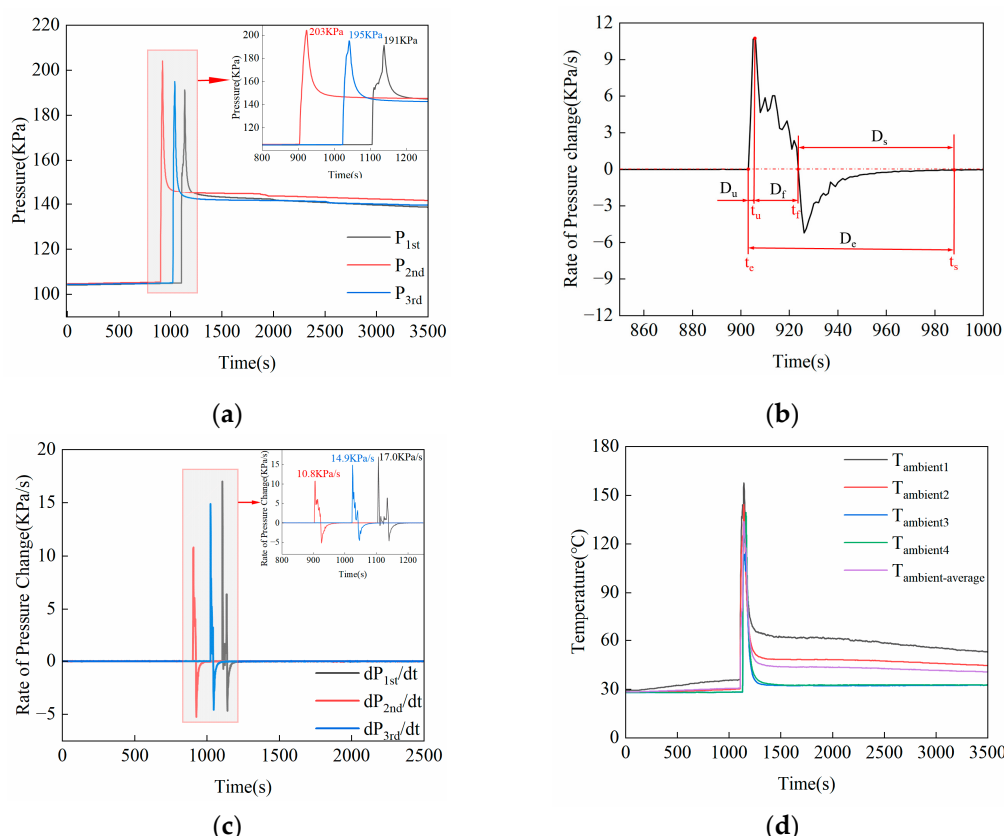
**Figure 6.** Sound and video signals during thermal runaway. (a) Amplitude of sound signal during thermal runaway. (b) Image of safety valve opening during thermal runaway. (c) Image of flame generation at the start of thermal runaway combustion. (d) Image after completion of thermal runaway ejection.

Figure 6a illustrates the process from the opening of the safety valve to the complete ejection of the battery. The moment when the sound starts is defined as time 0. During the time intervals of 0–6 s and 24–32 s, the sound amplitude is larger, with a relatively smaller amplitude in between. This is because, during the thermal runaway process, the heating plate first triggers thermal runaway in the first wound core, and then the thermal runaway propagates to the second wound core, resulting in two high-amplitude periods. The total duration of the sound signal is 34 s. Sound is only produced during high-speed ejection; low-speed ejection generally does not produce sound.

Figure 6b shows the image inside the chamber at the moment the sound starts, indicating the initial opening of the safety valve. Figure 6c shows the image when the thermal runaway ejection products begin to burn. Figure 6d shows the image inside the chamber at the moment the ejection sound disappears, indicating that the ejection has essentially ended and the chamber is filled with solid particle smoke. Therefore, the thermal runaway process involves the accumulation of battery heat to a certain threshold, partial opening of the safety valve, the beginning of gas ejection through the safety valve, generation of airflow noise, and as the reaction progresses, intense reactions and jet combustion occur. After a period of sustained combustion, the airflow noise ceases, the thermal runaway ends, and the flames extinguish. By capturing images of the battery and monitoring the light intensity of the flames, a low-cost early warning method for battery thermal runaway can be achieved [60–62].

### 3.4. Pressure Changes and Gas Production

To investigate the gas production rate of the NCM811 battery during thermal runaway in an oxygen-free environment, the battery was tested under a nitrogen atmosphere, and the pressure changes inside the chamber were recorded, as shown in Figure 7.



**Figure 7.** Pressure and temperature inside the experimental chamber. (a) Pressure changes during three experiments. (b) Segmentation of ejection phases. (c) Rate of pressure change inside the chamber. (d) Ambient temperature inside the chamber.

Figure 7a shows the pressure changes inside the chamber during the three experiments. During the triggering of thermal runaway, the pressure inside the chamber increased rapidly [35,63–66], reaching a peak of 203 KPa before quickly dropping and stabilizing at 143 KPa. The presence of a single pressure peak in this experiment indicates that the thermal runaway process involved only one ejection event.

Figure 7b illustrates the rate of pressure change inside the chamber during the first experiment. According to the segmentation of the ejection process proposed in the reference [67], the gas ejection stage ( $D_e$ ) of thermal runaway is divided into three phases:

1. Ultra-High-Speed Ejection Phase ( $D_u$ ): The time from the start of thermal runaway ejection ( $t_e$ ) to the moment of maximum ejection rate ( $t_u$ );
2. High-Speed Ejection Phase ( $D_f$ ): The time from the moment of maximum ejection rate ( $t_u$ ) to the moment when the ejection rate drops to zero ( $t_f$ );
3. Slow Ejection Phase ( $D_s$ ): The time from the moment when the ejection rate drops to zero ( $t_f$ ) to the end of the ejection ( $t_s$ ).

Figure 7c shows the rate of pressure change during the three experiments. Based on the segmentation of the ejection phases, the durations of the ejection phases for the three experiments are listed in Table 2.

**Table 2.** Duration of each ejection phase and maximum pressure change rate in the three experiments.

Experiment	$D_u$ (s)	$D_f$ (s)	$D_s$ (s)	$D_e$ (s)	$(dP/dt)_{max}$ (Kpa/s)
1st	2	32	47	81	17
2nd	3	18	53	74	10.8
3rd	2	17	53	72	14.8
Average	2.3	22.3	51	75.7	14.2

To calculate the gas production during thermal runaway, the ideal gas law Equation (2) is introduced in this study. By rearranging and transforming the equation, Formula (3) can be obtained.

$$PV = nRT \quad (2)$$

$$n = \frac{PV}{RT_{\text{ambient-average}}} - \frac{P_0V}{RT_0} \quad (3)$$

In the formula:

- $P$  is the pressure inside the chamber, in units of Pa;
- $P_0$  is the initial pressure inside the chamber, in units of Pa;
- $V$  is the volume of the experimental chamber, in units of  $\text{m}^3$ ;
- $n$  is the amount of gas in the chamber, in units of mol;
- $R$  is the ideal gas constant, with a value of 8.31441 J/(mol·K);
- $T_0$  is the ambient temperature at the start of the experiment, in units of K;
- $T_{\text{ambient-average}}$  is the average temperature of the four environmental monitoring points inside the experimental chamber, in units of K.

Based on the above formulas and the ambient temperature shown in Figure 7d, the amount of gas produced during the battery thermal runaway can be calculated. The data from the three experiments are shown in Table 3.

**Table 3.** Gas production and parameters from the three experiments.

Experiment	$P$ (Pa)	$T_{\text{ambient-average}}$ (K)	$T_{\text{ambient-max}}$ (K)	$n$ (mol)	$n_{Ah}$ (mol/Ah)
1st	143,200	321.45	465.7	13.3	0.085
2nd	144,889	318.87	453.2	14.4	0.092
3rd	141,911	314.62	438.6	14.0	0.090
Average	143,333	318.31	452.5	13.9	0.089

In the experiment, the distance from the top of the battery to the top of the chamber is approximately 800 mm. During thermal runaway, the jet reflects off the chamber walls and fills the entire container, causing the ambient temperature to rise. In the three experiments, the highest ambient temperature reached 465.7 K (192.5 °C), which is within the operating temperature range of the pressure sensor (−40 °C to 200 °C). Therefore, the 1000 L experimental chamber can accurately measure the pressure changes within the chamber.

Because gas production is closely related to battery capacity, a parameter called unit capacity molar amount,  $n_{Ah}$ , is defined to evaluate the gas production per unit capacity. The calculation formula is as follows:

$$n_{Ah} = \frac{n}{Capacity} \quad (4)$$

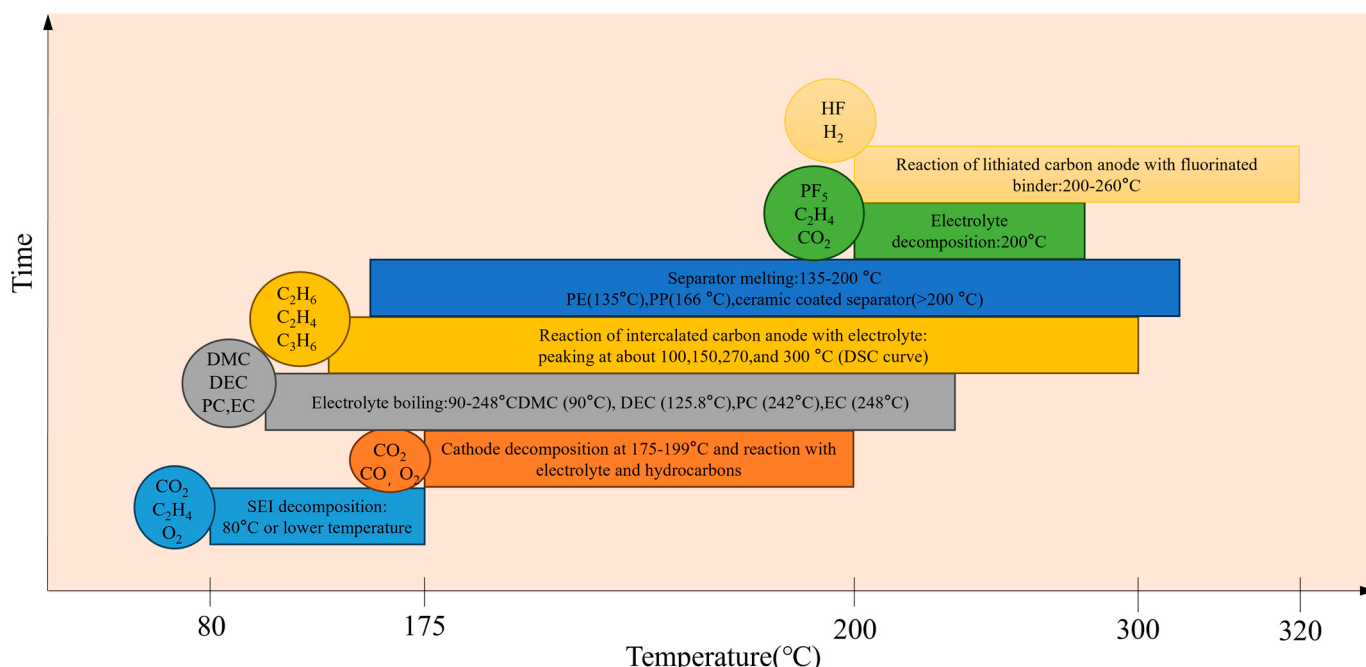
In the formula:

- $n_{Ah}$  represents the molar amount of gas produced per unit capacity, in mol/Ah;
- $n$  represents the total amount of gas produced by the battery, in mol;
- Capacity represents the battery capacity, in Ah.

Based on the above formula, the unit capacity molar amount for the 156 Ah NCM811 battery from the three experiments is 0.089 mol/Ah.

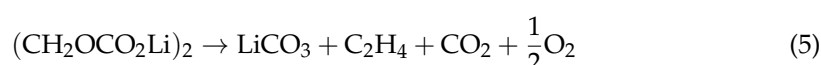
Based on the research by Shen and Yang et al. [5,48], the main gas components produced during the thermal runaway of 811 ternary lithium batteries in a nitrogen atmosphere are CO<sub>2</sub> (30.75%), H<sub>2</sub> (23.96%), CO (22.92%), C<sub>2</sub>H<sub>4</sub> (15.71%), and CH<sub>4</sub> (5.3%).

Figure 8 illustrates the relationship between gas generation and temperature during the thermal runaway of the battery. The primary processes involved are as follows:

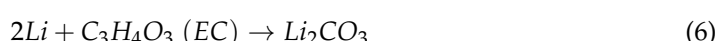


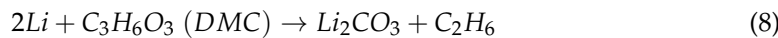
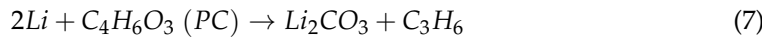
**Figure 8.** Time Series of Gas Generation [68].

SEI Film Decomposition:

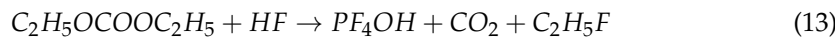
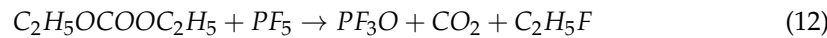
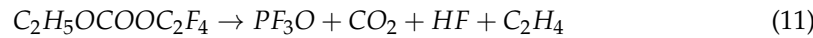


As the temperature increases, the active lithium in the electrodes begins to react with the electrolyte:





The electrolyte simultaneously undergoes its own decomposition reactions:



According to Li et al.'s theory on the ignition triangle of gas generation during battery thermal runaway, the upper flammable limit (UFL) and lower flammable limit (LFL) curves of gases produced by ternary lithium batteries exhibit a peninsula shape [69]. The flammable range remains relatively constant before sharply decreasing, forming a triangular shape. In this study, experiments conducted in a nitrogen atmosphere effectively extend the safety threshold during the thermal runaway process of lithium batteries.

### 3.5. Battery Morphological Characteristics

NCM811 lithium batteries have high energy density, and their thermal runaway generates a significant amount of heat. This heat leads to chemical reactions between the electrode materials and the electrolyte, producing a large amount of flammable gas, causing the battery casing to become damaged. To investigate the morphological characteristics of the battery after thermal runaway [70,71], the remnants of the battery from the three experiments were analyzed. Figure 8 shows the battery's morphology before and after thermal runaway.

Figure 9a shows the external appearance of the battery before thermal runaway. Figure 9b–d display the morphology of the battery after thermal runaway. It can be observed that 2/3 of the large surface area of the battery casing is damaged and melted, exposing the internal copper foils. The casing near the safety valve is completely broken, and jet grooves formed by ejection are present near the safety valve, with jet angles between 45 and  $-45$  degrees.

Experimental data indicate that the inflection point of the pressure increase inside the experimental chamber caused by the valve opening and the rapid temperature rise occur almost simultaneously. At the 1106 s mark, the battery's safety valve opens, and the highest temperature at the T<sub>front</sub> position is 257.2 °C, which is far below the melting point of the battery's aluminum casing at 660.3 °C. Therefore, the battery casing will not be damaged before the safety valve opens. After the safety valve opens, using the aluminum casing's melting point of 660.3 °C as the dividing line:

1. When the T<sub>front</sub> position temperature is below 660.3 °C, the battery casing remains intact, and all the jet is expelled through the safety valve;
2. When the T<sub>front</sub> position temperature exceeds 660.3 °C, the battery casing will be damaged, and the jet may be expelled from both the safety valve and the damaged area.

The damage and melting of the battery casing indicate that the intense reactions of the internal electrode active materials and the electrolyte produced a large amount of heat, with temperatures exceeding the melting point of aluminum (660.4 °C), causing the aluminum casing and internal aluminum foils to melt. The exposed internal copper foils show no signs of melting, indicating that the internal thermal runaway temperature did not reach the melting point of copper (1083.4 °C). Therefore, the internal thermal runaway temperature is between 660.4 °C and 1083.4 °C. The jet grooves are mainly distributed at angles of  $\pm 45$  degrees, indicating that the jet direction is within this range. Placing temperature monitoring points directly above the ejection outlet may result in inaccurate jet temperature

measurements. The jet grooves are mainly distributed at angles of  $\pm 45$  degrees, indicating that the jets are ejected at these angles. This occurs because, during the initial phase of the ejection, the internal structure of the battery restricts the jet to a  $45^\circ$  angle. As the reaction progresses, the temperature inside the battery rapidly increases, causing damage to the internal structure. This results in the airflow starting to damage the central part of the battery as well. Therefore, setting the temperature measurement point directly above the nozzle may result in inaccurate jet temperature measurements.

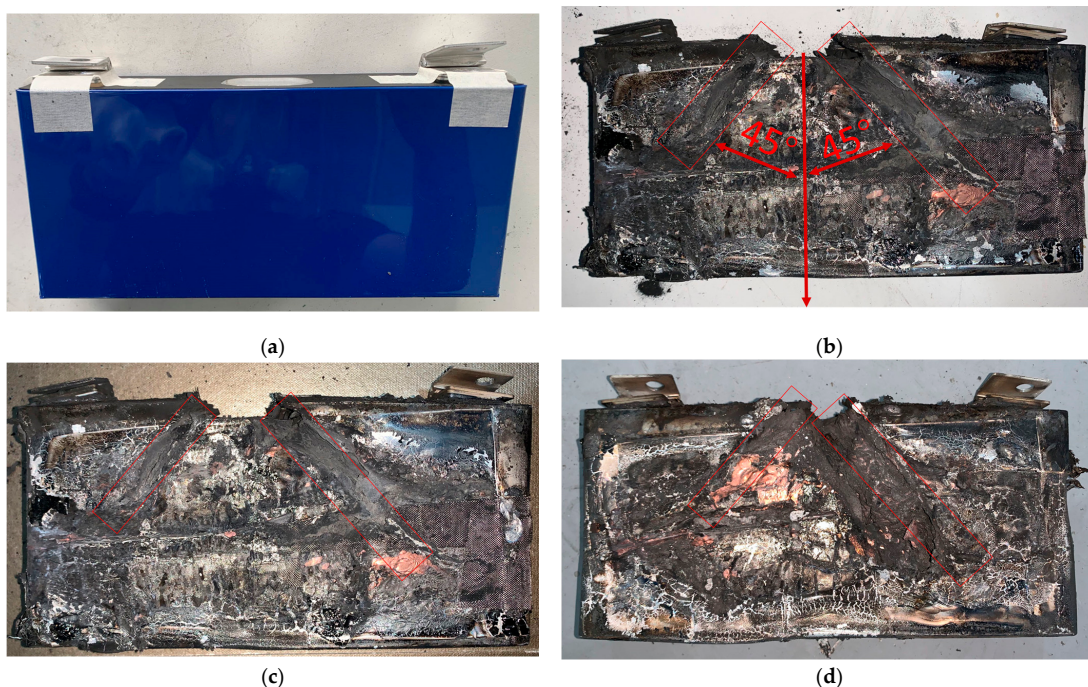


**Figure 9.** Battery photographs. (a) Battery before thermal runaway. (b) Battery remains after thermal runaway in the first experiment. (c) Battery remains after thermal runaway in the second experiment. (d) Battery remains after thermal runaway in the third experiment.

#### 4. Conclusions

In this study, the aim was to investigate the jetting behavior of ternary lithium batteries at 100% SOC under a nitrogen atmosphere (99.75%) during thermal runaway. This was achieved by laterally heating the battery with a 400 W heating plate, triggering thermal runaway in a ternary lithium battery with a cathode material of  $\text{Li}(\text{Ni}_{0.8}\text{Co}_{0.1}\text{Mn}_{0.1})\text{O}_2$  and a capacity of 156 Ah. Through data analysis, the battery surface temperature, jet temperature, pressure changes, acoustic signal changes, and post-thermal runaway morphological characteristics were obtained. The main conclusions are as follows:

1. During the thermal runaway of the 811 ternary lithium battery, the front surface temperature of the battery can reach  $851.8\text{--}943.7\text{ }^\circ\text{C}$ , and the back surface temperature can reach  $658.3\text{--}694.1\text{ }^\circ\text{C}$ , both exceeding the melting point of the aluminum casing ( $660.4\text{ }^\circ\text{C}$ ). This melting can cause inaccuracies in temperature measurements. The temperatures of the bottom surface and the small side surfaces are lower than the aluminum melting point, and the order of the appearance of thermal runaway temperature inflection points is: Time( $T_{\text{front}}$ ) = Time( $T_{\text{bottom}}$ ) = Time( $T_{\text{left}}$ ) < Time( $T_{\text{right}}$ ) < Time( $T_{\text{back}}$ ). From the perspective of thermal runaway early warning, monitoring the temperature at the bottom surface and the small side surface near the battery anode is more accurate;
2. The highest jet temperatures at 50 mm, 150 mm, and 250 mm above the safety valve were  $356.9\text{ }^\circ\text{C}$ ,  $302.7\text{ }^\circ\text{C}$ , and  $216.5\text{ }^\circ\text{C}$ , respectively. This indicates that the further from the outlet, the lower the jet temperature. The temperature rise rates at these

- three points were  $77.1\text{ }^{\circ}\text{C}/\text{s}$ ,  $40.9\text{ }^{\circ}\text{C}/\text{s}$ , and  $26.9\text{ }^{\circ}\text{C}/\text{s}$ , respectively, showing that the temperature rise rate is inversely proportional to the distance from the safety valve;
3. Based on acoustic and image signals, it was found that there are two intensive sound amplitude stages during the ternary battery ejection process, which are closely related to the number of battery wound cores;
  4. Under the conditions of this experiment, the average gas production of the battery was  $0.089\text{ mol/Ah}$ . Based on the pressure data from the first experiment, one ejection process was observed, which included ultra-high-speed ejection (2 s), high-speed ejection (32 s), and slow ejection (47 s) stages. Combined with the ejection process captured by the acoustic signals (34 s), it indicates that exhaust sounds are produced during the ultra-high-speed and high-speed ejection stages due to high-speed airflow impact, while no exhaust sound is produced during the slow ejection stage. This has significant research value for using acoustic signals to provide early warnings of battery thermal runaway;
  5. Based on the post-thermal runaway remnants, it was found that the grooves caused by airflow impact are mainly located at  $\pm 45^{\circ}$ . Therefore, when measuring the jet temperature during thermal runaway, monitoring points should be arranged within the  $\pm 45^{\circ}$  range.

**Funding:** This research received no external funding.

**Data Availability Statement:** The data are available through appropriate requests.

**Conflicts of Interest:** The author declares no conflicts of interest.

## References

1. Dong, Y.; Meng, J.; Sun, X.; Zhao, P.; Sun, P.; Zheng, B. Experimental Study on Effects of Triggering Modes on Thermal Runaway Characteristics of Lithium-Ion Battery. *World Electr. Veh. J.* **2023**, *14*, 270. [[CrossRef](#)]
2. Du, Q.; Fang, Z. Analysis of the Thermal Behavior of a Lithium Cell Undergoing Thermal Runaway. *Fluid Dyn. Mater. Process.* **2021**, *17*, 887–898. [[CrossRef](#)]
3. Gao, F.; Yang, K.; Wang, C.; Liu, W.; Zhu, Y. Experimental Study on Thermal Runaway of LiFePO<sub>4</sub>/C Battery under Heating Condition. *IOP Conf. Ser. Earth Environ. Sci.* **2020**, *546*, 042025. [[CrossRef](#)]
4. Ji, C.; Zhang, S.; Wang, B.; Sun, J.; Zhang, Z.; Liu, Y. Study on Thermal Safety of the Overcharged Lithium-Ion Battery. *Fire Technol.* **2023**, *59*, 1089–1114. [[CrossRef](#)]
5. Shen, H.; Wang, H.; Li, M.; Li, C.; Zhang, Y.; Li, Y.; Yang, X.; Feng, X.; Ouyang, M. Thermal Runaway Characteristics and Gas Composition Analysis of Lithium-Ion Batteries with Different LFP and NCM Cathode Materials under Inert Atmosphere. *Electronics* **2023**, *12*, 1603. [[CrossRef](#)]
6. Lai, Y.; Yang, K.; Liu, H.; Gao, F.; Zhang, M.; Xu, W. A Probe into the Accuracy of Thermal Runaway Simulation Model of Lithium-ion Battery under Adiabatic Condition. *IOP Conf. Ser. Earth Environ. Sci.* **2021**, *680*, 012009. [[CrossRef](#)]
7. Li, Q.; Yu, J.; Liu, G.; Ma, X.; Si, W.; Hu, X.; Zhu, G.; Liu, T. Study on the Effectiveness of Water Mist on Suppressing Thermal Runaway in LiFePO<sub>4</sub> Batteries. *Crystals* **2023**, *13*, 1346. [[CrossRef](#)]
8. Li, X.; Liu, X.; Zhang, Y. Research and Development of Fire Alarm Detection Device for Lithium Ion Battery Based on Strain Measurement. *IOP Conf. Ser. Earth Environ. Sci.* **2020**, *605*, 012005. [[CrossRef](#)]
9. Li, Y.; Jiang, L.; Huang, Z.; Jia, Z.; Qin, P.; Wang, Q. Pressure Effect on the Thermal Runaway Behaviors of Lithium-Ion Battery in Confined Space. *Fire Technol.* **2023**, *59*, 1137–1155. [[CrossRef](#)]
10. Available online: <https://homeland.house.gov/2024/02/15/subcommittee-chairman-desposito-delivers-opening-statement-in-hearing-on-fire-hazards-lithium-ion-battery-risks/> (accessed on 16 June 2024).
11. Miao, H. Research on accurate fire detection & early warning model for lithium-ion battery packs. *J. Phys. Conf. Ser.* **2024**, *2703*, 012068. [[CrossRef](#)]
12. Qian, F.; Wang, H.; Li, M.; Cheng, L.; Shen, H.; Wang, J.; Li, Y.; Ouyang, M. Thermal Runaway Vent Gases from High-Capacity Energy Storage LiFePO<sub>4</sub> Lithium Iron. *Energies* **2023**, *16*, 3485. [[CrossRef](#)]
13. Seyed Saeed, M.; Ziebert, C.; Mousa, M. Thermal Characteristics and Safety Aspects of Lithium-Ion Batteries: An In-Depth Review. *Symmetry* **2023**, *15*, 1925. [[CrossRef](#)]
14. Sun, J.; Li, G.; Xie, S.; He, Y. The Influence of Airflow Rate on the Thermal Runaway Propagation Characteristics of Lithium-Ion Batteries in a Low-Pressure Environment. *Fire Technol.* **2022**, *58*, 3553–3576. [[CrossRef](#)]
15. Wang, K.; Ouyang, D.; Qian, X.; Yuan, S.; Chang, C.; Zhang, J.; Liu, Y. Early Warning Method and Fire Extinguishing Technology of Lithium-Ion Battery Thermal Runaway: A Review. *Energies* **2023**, *16*, 2960. [[CrossRef](#)]

16. Wang, L.; Yang, X.; Wang, Q.; Tian, H. Research on Thermal Out of Control of Lithium Battery in New Energy Vehicles. *IOP Conf. Ser. Earth Environ. Sci.* **2020**, *446*, 022038. [[CrossRef](#)]
17. Wang, Z.; Tang, X.; Zhou, Y.; Huang, H.; Dai, H. Experimental and Modeling Analysis of Thermal Runaway for LiNi<sub>0.5</sub>Mn<sub>0.3</sub>Co<sub>0.2</sub>O<sub>2</sub>/Graphite Pouch Cell Triggered by Surface Heating. *Energies* **2024**, *17*, 826. [[CrossRef](#)]
18. Zhang, G.; Li, Z.; Wang, H.; Yuan, D. Study on the Suppression Effect of Cryogenic Cooling on Thermal Runaway of Ternary Lithium-Ion Batteries. *Fire* **2022**, *5*, 182. [[CrossRef](#)]
19. Li, J.; Gao, P.; Tong, B.; Cheng, Z.; Cao, M.; Mei, W.; Wang, Q.; Sun, J.; Qin, P. Revealing the mechanism of pack ceiling failure induced by thermal runaway in NCM batteries: A coupled multiphase fluid-structure interaction model for electric vehicles. *eTransportation* **2024**, *20*, 100335. [[CrossRef](#)]
20. Liu, Z.; Zhu, Y.; Li, R.; Tao, C.; Chen, Z.; Liu, T.; Li, Y. The experimental investigation of thermal runaway characteristics of lithium battery under different concentrations of heptafluoropropane and air. *J. Energy Storage* **2024**, *84*, 110828. [[CrossRef](#)]
21. Xie, H.J.; Sun, J.; Li, J.G.; Zhou, T.; Wei, S.P.; Yi, Z.H. Lithium-Ion Battery Thermal Runaway Electro-Thermal Triggering Method and Toxicity Analysis. *IOP Conf. Ser. Earth Environ. Sci.* **2021**, *701*, 012007. [[CrossRef](#)]
22. Bugryniec, P.J.; Resendiz, E.G.; Nwophoke, S.M.; Khanna, S.; James, C.; Brown, S.F. Review of gas emissions from lithium-ion battery thermal runaway failure—Considering toxic and flammable compounds. *J. Energy Storage* **2024**, *87*, 111288. [[CrossRef](#)]
23. Wei, G.; Huang, R.; Zhang, G.; Jiang, B.; Zhu, J.; Guo, Y.; Han, G.; Wei, X.; Dai, H. A comprehensive insight into the thermal runaway issues in the view of lithium-ion battery intrinsic safety performance and venting gas explosion hazards. *Appl. Energy* **2023**, *349*, 121651. [[CrossRef](#)]
24. Zhang, Q.; Yang, K.; Niu, J.; Liu, T.; Hu, J. Research on the lower explosion limit of thermal runaway gas in lithium batteries under high-temperature and slight overcharge conditions. *J. Energy Storage* **2023**, *79*, 109976. [[CrossRef](#)]
25. Chen, M.; He, Y.; De Zhou, C.; Richard, Y.; Wang, J. Experimental Study on the Combustion Characteristics of Primary Lithium Batteries Fire. *Fire Technol.* **2014**, *52*, 365–385. [[CrossRef](#)]
26. Jia, L.; Wang, D.; Yin, T.; Li, X.; Li, L.; Dai, Z.; Zheng, L. Experimental Study on Thermal-Induced Runaway in High Nickel Ternary Batteries. *ACS Omega* **2022**, *7*, 14562–14570. [[CrossRef](#)]
27. Thomas, F.; Mills, G.; Howe, R.; Zobell, J. Lithium Battery Fires: Implications for Air Medical Transport. *Air Med. J.* **2012**, *31*, 242–248. [[CrossRef](#)]
28. Wei, D.; Zhang, M.; Zhu, L.; Hu, C.; Huang, W.; Yao, J.; Yuan, Z.; Xu, C.; Feng, X. Study on Thermal Runaway Behavior of Li-Ion Batteries Using Different Abuse Methods. *Batteries* **2022**, *8*, 201. [[CrossRef](#)]
29. Ohneseit, S.; Finster, P.; Floras, C.; Lubenau, N.; Uhlmann, N.; Seifert, H.J.; Ziebert, C. Thermal and Mechanical Safety Assessment of Type 21700 Lithium-Ion Batteries with NMC, NCA and LFP Cathodes—Investigation of Cell Abuse by Means of Accelerating Rate Calorimetry (ARC). *Batteries* **2023**, *9*, 237. [[CrossRef](#)]
30. Han, Z.; Zhao, L.; Zhao, J.; Xu, J.; Liu, H.; Chen, M. An Experimental Study on the Thermal Runaway Propagation of Cycling Aged Lithium-Ion Battery Modules. *Fire* **2024**, *7*, 119. [[CrossRef](#)]
31. Deng, J.; Chen, B.; Lu, J.; Zhou, T.; Wu, C. Thermal runaway and combustion characteristics, risk and hazard evaluation of lithium-iron phosphate battery under different thermal runaway triggering modes. *Appl. Energy* **2024**, *368*, 123451. [[CrossRef](#)]
32. Zhou, Z.; Li, M.; Zhou, X.; Li, L.; Ju, X.; Yang, L. Investigating thermal runaway triggering mechanism of the prismatic lithium iron phosphate battery under thermal abuse. *Renew. Energy* **2023**, *220*, 119674. [[CrossRef](#)]
33. Li, C.; Wang, H.; Han, X.; Wang, Y.; Wang, Y.; Zhang, Y.; Feng, X.; Ouyang, M. An Experimental Study on Thermal Runaway Behavior for High-Capacity Li(Ni<sub>0.8</sub>Co<sub>0.1</sub>Mn<sub>0.1</sub>)O<sub>2</sub> Pouch Cells at Different State of Charges. *J. Electrochem. Energy Convers. Storage* **2021**, *18*, 021012. [[CrossRef](#)]
34. Liao, Z.; Zhang, S.; Li, K.; Zhao, M.; Qiu, Z.; Han, D.; Zhang, G.; Habetler, T.G. Hazard analysis of thermally abused lithium-ion batteries at different state of charges. *J. Energy Storage* **2019**, *27*, 101065. [[CrossRef](#)]
35. Sun, Q.; Liu, H.; Zhi, M.; Chen, X.; Lv, P.; He, Y. Thermal characteristics of thermal runaway for pouch lithium-ion battery with different state of charges under various ambient pressures. *J. Power Sources* **2022**. [[CrossRef](#)]
36. Wu, H.; Chen, S.; Hong, Y.; Xu, C.; Zheng, Y.; Jin, C.; Chen, K.; He, Y.; Feng, X.; Wei, X.; et al. Thermal safety boundary of lithium-ion battery at different state of charge. *J. Energy Chem.* **2023**, *91*, 59–72. [[CrossRef](#)]
37. Doose, S.; Hahn, A.; Fischer, S.; Müller, J.; Haselrieder, W.; Kwade, A. Comparison of the consequences of state of charge and state of health on the thermal runaway behavior of lithium ion batteries. *J. Energy Storage* **2023**, *62*, 106837. [[CrossRef](#)]
38. Liu, J.; Wang, Z.; Bai, J.; Gao, T.; Mao, N. Heat generation and thermal runaway mechanisms induced by overcharging of aged lithium-ion battery. *Appl. Therm. Eng.* **2022**, *212*, 118565. [[CrossRef](#)]
39. Xiao, Y.; Wen, J.; Yao, L.; Zheng, J.; Fang, Z.; Shen, Y. A comprehensive review of the lithium-ion battery state of health prognosis methods combining aging mechanism analysis. *J. Energy Storage* **2023**, *65*, 107347. [[CrossRef](#)]
40. Zhang, L.; Liu, L.; Terekhov, A.; Warnberg, D.; Zhao, P. Thermal runaway of Li-ion battery with different aging histories. *Process Saf. Environ. Prot.* **2024**, *185*, 910–917. [[CrossRef](#)]
41. Zhang, L.; Liu, L.; Yang, S.; Xie, Z.; Zhang, F.; Zhao, P. Experimental investigation on thermal runaway suspension with battery health retention. *Appl. Therm. Eng.* **2023**, *225*, 120239. [[CrossRef](#)]
42. Jin, C.; Sun, Y.; Wang, H.; Zheng, Y.; Wang, S.; Rui, X.; Xu, C.; Feng, X.; Wang, H.; Ouyang, M. Heating power and heating energy effect on the thermal runaway propagation characteristics of lithium-ion battery module: Experiments and modeling. *Appl. Energy* **2022**, *312*, 118760. [[CrossRef](#)]

43. Meng, D.; Wang, X.; Chen, M.; Wang, J. Effects of environmental temperature on the thermal runaway of lithium-ion batteries during charging process. *J. Loss Prev. Process Ind.* **2023**, *83*, 105084. [[CrossRef](#)]
44. Parhizi, M.; Ahmed, M.B.; Jain, A. Determination of the core temperature of a Li-ion cell during thermal runaway. *J. Power Sources* **2017**, *370*, 27–35. [[CrossRef](#)]
45. Liu, C.; Huang, Q.; Zheng, K.; Qin, J.; Zhou, D.; Wang, J. Impact of Lithium Salts on the Combustion Characteristics of Electrolyte under Diverse Pressures. *Energies* **2020**, *13*, 5373. [[CrossRef](#)]
46. Teslenko, V.S.; Drozhzhin, A.P.; Medvedev, N.; Manzhalei, V.I. Initiation of combustion of a gas mixture by an electric explosion of an electrolyte. *Combust. Explos. Shock. Waves* **2012**, *48*, 730–733. [[CrossRef](#)]
47. Yang, W.; Zhang, Y.; Deng, J.; Chen, J.; Ji, X.; Wu, H.; Zhao, J. Experimental study on combustion characteristics of electrolyte pool fire. *J. Energy Storage* **2024**, *93*, 112214. [[CrossRef](#)]
48. Yang, X.; Wang, H.; Li, M.; Li, Y.; Li, C.; Zhang, Y.; Chen, S.; Shen, H.; Qian, F.; Feng, X.; et al. Experimental Study on Thermal Runaway Behavior of Lithium-Ion Battery and Analysis of Combustible Limit of Gas Production. *Batteries* **2022**, *8*, 250. [[CrossRef](#)]
49. Zhang, F.; Feng, X.; Xu, C.; Jiang, F.; Ouyang, M. Thermal runaway front in failure propagation of long-shape lithium-ion battery. *Int. J. Heat Mass Transf.* **2021**, *182*, 121928. [[CrossRef](#)]
50. Ma, Z.; Huo, Q.; Wang, W.; Zhang, T. Voltage-temperature aware thermal runaway alarming framework for electric vehicles via deep learning with attention mechanism in time-frequency domain. *Energy* **2023**, *278*, 127747. [[CrossRef](#)]
51. Zhang, Q.; Liu, T.; Wang, Q. Experimental study on the influence of different heating methods on thermal runaway of lithium-ion battery. *J. Energy Storage* **2021**, *42*, 103063. [[CrossRef](#)]
52. Liu, P.; Li, Y.; Mao, B.; Chen, M.; Huang, Z.; Wang, Q. Experimental study on thermal runaway and fire behaviors of large format lithium iron phosphate battery. *Appl. Therm. Eng.* **2021**, *192*, 116949. [[CrossRef](#)]
53. Wang, G.; Ping, P.; Zhang, Y.; Zhao, H.; Lv, H.; Gao, X.; Gao, W.; Kong, D. Modeling thermal runaway propagation of lithium-ion batteries under impacts of ceiling jet fire. *Process Saf. Environ. Prot.* **2023**, *175*, 524–540. [[CrossRef](#)]
54. Zhao, R.; Lai, Z.; Li, W.; Ye, M.; Yu, S. Development of a coupled model of heat generation and jet flow of lithium-ion batteries during thermal runaway. *J. Energy Storage* **2023**, *63*, 107048. [[CrossRef](#)]
55. Zhou, W.; Zhao, H.; Wu, D.; Yang, Y.; Yuan, C.; Li, G. Inhibition effect of inert gas jet on gas and hybrid explosions caused by thermal runaway of lithium-ion battery. *J. Loss Prev. Process Ind.* **2024**, *90*, 105336. [[CrossRef](#)]
56. Zhou, Z.; Zhou, X.; Wang, D.; Li, M.; Wang, B.; Yang, L.; Cao, B. Experimental analysis of lengthwise/transversal thermal characteristics and jet flow of large-format prismatic lithium-ion battery. *Appl. Therm. Eng.* **2021**, *195*, 117244. [[CrossRef](#)]
57. Zou, K.; Chen, X.; Ding, Z.; Gu, J.; Lu, S. Jet behavior of prismatic lithium-ion batteries during thermal runaway. *Appl. Therm. Eng.* **2020**, *179*, 115745. [[CrossRef](#)]
58. Golubkov, A.W.; Planteu, R.; Krohn, P.; Rasch, B.; Brunnsteiner, B.; Thaler, A.; Hacker, V. Thermal runaway of large automotive Li-ion batteries. *RSC Adv.* **2018**, *8*, 40172–40186. [[CrossRef](#)]
59. Su, T.; Lyu, N.; Zhao, Z.; Wang, H.; Jin, Y. Safety warning of lithium-ion battery energy storage station via venting acoustic signal detection for grid application. *J. Energy Storage* **2021**, *38*, 102498. [[CrossRef](#)]
60. Kong, D.; Lv, H.; Ping, P.; Wang, G. A review of early warning methods of thermal runaway of lithium ion batteries. *J. Energy Storage* **2023**, *64*, 107073. [[CrossRef](#)]
61. Nishant Ranjan Sinha, K.; Ranjan, D.; Raza, M.Q.; Kumar, N.; Kaner, S.; Thakur, A.; Raj, R. In-situ acoustic detection of critical heat flux for controlling thermal runaway in boiling systems. *Int. J. Heat Mass Transf.* **2019**, *138*, 135–143. [[CrossRef](#)]
62. Wang, Z.; Zhu, L.; Liu, J.; Wang, J.; Yan, W. Gas Sensing Technology for the Detection and Early Warning of Battery Thermal Runaway: A Review. *Energy Fuels* **2022**, *36*, 6038–6057. [[CrossRef](#)]
63. Chen, S.; Wang, Z.; Yan, W.; Liu, J. Investigation of impact pressure during thermal runaway of lithium ion battery in a semi-closed space. *Appl. Therm. Eng.* **2020**, *175*, 115429. [[CrossRef](#)]
64. Dubaniewicz, T.H.; Zlochower, I.; Barone, T.; Thomas, R.; Yuan, L. Thermal Runaway Pressures of Iron Phosphate Lithium-Ion Cells as a Function of Free Space within Sealed Enclosures. *Min. Metall. Explor.* **2020**, *38*, 539–547. [[CrossRef](#)]
65. Thomas, H.D.; Teresa, L.B.; Connor, B.B.; Richard, A.T. Comparison of thermal runaway pressures within sealed enclosures for nickel manganese cobalt and iron phosphate cathode lithium-ion cells. *J. Loss Prev. Process Ind.* **2022**, *76*, 104739. [[CrossRef](#)]
66. Xu, L.; Wang, S.; Li, Y.; Li, Y.; Sun, J.; Zhao, F.; Wang, H.; Wang, Y.; Xu, C.; Feng, X. Thermal runaway propagation behavior and gas production characteristics of NCM622 battery modules at different state of charge. *Process Saf. Environ. Prot.* **2024**, *185*, 267–276. [[CrossRef](#)]
67. Zhang, Y.; Wang, H.; Li, W.; Li, C.; Ouyang, M. Quantitative analysis of eruption process of abused prismatic Ni-rich automotive batteries based on in-chamber pressure. *J. Energy Storage* **2020**, *31*, 101617. [[CrossRef](#)]
68. Wang, H.; Zhang, Y.; Li, W.; Gao, Z.; Zhang, B.; Ouyang, M. Experimental study on the cell-jet temperatures of abused prismatic Ni-rich automotive batteries under medium and high states of charge. *Appl. Therm. Eng.* **2022**, *202*, 117859. [[CrossRef](#)]
69. Li, W.; Wang, H.; Zhang, Y.; Ouyang, M. Flammability characteristics of the battery vent gas: A case of NCA and LFP lithium-ion batteries during external heating abuse. *J. Energy Storage* **2019**, *24*, 100775. [[CrossRef](#)]

70. Gong, Z.; Gu, C.; Sun, J.; Wang, H.; Li, Y.; Zhou, X.; Jia, Y.; Han, D. Experimental study on thermal runaway characteristic and residue of  $\text{Li}(\text{Ni}_{0.8}\text{Co}_{0.1}\text{Mn}_{0.1})\text{O}_2$  lithium-ion batteries induced by overcharge. *J. Energy Storage* **2023**, *68*, 107705. [[CrossRef](#)]
71. Wei, N.; Li, M. Experimental study of thermal runaway process of 256Ah prismatic nickel-rich battery. *Front. Energy Res.* **2023**, *11*, 1230429. [[CrossRef](#)]

**Disclaimer/Publisher's Note:** The statements, opinions and data contained in all publications are solely those of the individual author(s) and contributor(s) and not of MDPI and/or the editor(s). MDPI and/or the editor(s) disclaim responsibility for any injury to people or property resulting from any ideas, methods, instructions or products referred to in the content.